ARTICLE

doi:10.1038/nature14685

Structure of the eukaryotic MCM complex at 3.8 Å

Ningning Li[1]*, Yuanliang Zhai[2,3]*, Yixiao Zhang[1], Wanqiu Li[1], Maojun Yang[1], Jianlin Lei[1], Bik-Kwoon Tye[2,4] & Ning Gao[1]

DNA replication in eukaryotes is strictly regulated by several mechanisms. A central step in this replication is the assembly of the heterohexameric minichromosome maintenance (MCM2–7) helicase complex at replication origins during G1 phase as an inactive double hexamer. Here, using cryo-electron microscopy, we report a near-atomic structure of the MCM2–7 double hexamer purified from yeast G1 chromatin. Our structure shows that two single hexamers, arranged in a tilted and twisted fashion through interdigitated amino-terminal domain interactions, form a kinked central channel. Four constricted rings consisting of conserved interior β-hairpins from the two single hexamers create a narrow passageway that tightly fits duplex DNA. This narrow passageway, reinforced by the offset of the two single hexamers at the double hexamer interface, is flanked by two pairs of gate-forming subunits, MCM2 and MCM5. These unusual features of the twisted and tilted single hexamers suggest a concerted mechanism for the melting of origin DNA that requires structural deformation of the intervening DNA.

For DNA to be replicated, two strands of the duplex DNA must be separated so that each can serve as a template for the synthesis of daughter strands. In both prokaryotes and eukaryotes, DNA unwinding is carried out by specialized helicases that encircle and translocate along one of the DNA strands[1]. However, the mechanisms for the initial melting or unwinding of origin DNA are markedly different[1,2]. In bacteria, the origin recognition protein DnaA initiates origin melting and then recruits hexameric helicase DnaB[3] to unwind DNA by translocation on the lagging strand in the 5′–3′ direction[2]. By contrast, in eukaryotes, the origin recognition complex first binds replication origins without effecting initial origin melting, and then loads two MCM2–7 (ref. 4) single hexamers with the help of the DNA replication proteins Cdc6 and Cdt1 onto double-stranded origin DNA to form a double hexamer[5,6]. This inactive assembly of proteins is known as the pre-replicative complex. Subsequent activation of MCM2–7 complex takes place in the S phase, and requires several factors and cell-cycle-specific kinases[7–11], resulting in the formation of an active replicative helicase, the Cdc45–MCM2–7–GINS (CMG) complex[12]. CMG translocates along the leading strand in a 3′–5′ direction to unwind duplex DNA (steric exclusion model)[13–17]. However, how origin DNA is melted before active replication elongation is unknown. This process probably requires the reconfiguration of MCM2–7 helicase, a complex molecular motor that has defied high-resolution structural analysis for decades. At present, much of the mechanistic insights came from low-resolution structures of the MCM2–7 complex in functional forms from different species[5,16,18–22], as well as crystal structures of simpler archaeal versions, in non-functional oligomers[23–25], truncations[26–29] or a chimaeric hexamer[30].

In this study, we purified the endogenous MCM2–7 double hexamer from G1 chromatin of budding yeast (Extended Data Fig. 1a–c), and determined its cryo-EM structure at an overall resolution of 3.8 Å (gold-standard Fourier shell correlation 0.143 criteria) (Extended Data Fig. 1k). Except for peripheral regions, the core of the map is better than 3.5 Å (Extended Data Fig. 1j), which enabled atomic model building for ~80% of sequences of this 1.2-megadalton (MDa) complex. Our structure reveals rich details for the organization of this large complex, and informs many functional aspects of this replicative helicase, particularly in the initial origin melting.

Overall structure and domain organization

A first glimpse of the structure is the tilted arrangement of two single hexamers, with a 14° wedge in between (Fig. 1a–c), a feature already noticed from low-resolution data of the MCM2–7 double hexamer[5,18] and the SV40 large tumour antigen[31]. The two single hexamers also have a twisted arrangement (Fig. 1a, side panel), resulting in the misalignment of two hexamer axes. The quality of the density map allowed an independent assignment of six subunits, being 2-6-4-7-3-5 (viewed from the carboxy-terminal domain (CTD) ring) (Fig. 1d), consistent with the well-established model[21,32,33]. Notably, when viewed from the single hexamer axis, the gravity centres of three major structural components—NTD-A (A subdomain of N-terminal domain (NTD)), oligonucleotide/oligosaccharide-binding (OB)-fold (C subdomain of NTD), and CTD—fall onto three eccentric circles (Fig. 1d). While the circles of NTD-As and OBs are nearly concentric, the CTD circle exhibits apparent rotational and translational offsets, indicating a relative shift and twist between the NTD and CTD rings within the single hexamer. Also, the NTD-As and OBs for each subunit are nearly vertically arranged (as indicated by their centres falling along on the same radial lines), with slight rotations in opposite directions for MCM4 and MCM5. Notably, the CTDs of all six subunits have left-handed twists to varying extents (Fig. 1d, f) with respect to their OBs and NTDs. Furthermore, the distances between neighbouring CTDs are different (Fig. 1e), showing a 4-Å difference between tightly (4:7, 7:3 and 5:2) and loosely (6:4, 3:5 and 2:6) packed groups. While six OBs form a plane perpendicular to the hexamer axis, the CTDs and NTD-As display marked axial variations (Fig. 1f, g).

Inter-hexamer interface

The head-to-head stacking of the two hexamers is largely mediated by their zinc-fingers (ZFs; B subdomain of NTD), as expected from

[1]Ministry of Education Key Laboratory of Protein Sciences, Center for Structural Biology, School of Life Sciences, Tsinghua University, Beijing 100084, China. [2]Division of Life Science, Hong Kong University of Science and Technology, Clear Water Bay, Kowloon, Hong Kong, China. [3]Institute for Advanced Study, Hong Kong University of Science and Technology, Clear Water Bay, Kowloon, Hong Kong, China. [4]Department of Molecular Biology and Genetics, College of Agriculture and Life Sciences, Cornell University, Ithaca, New York 14853, USA.
*These authors contributed equally to this work.

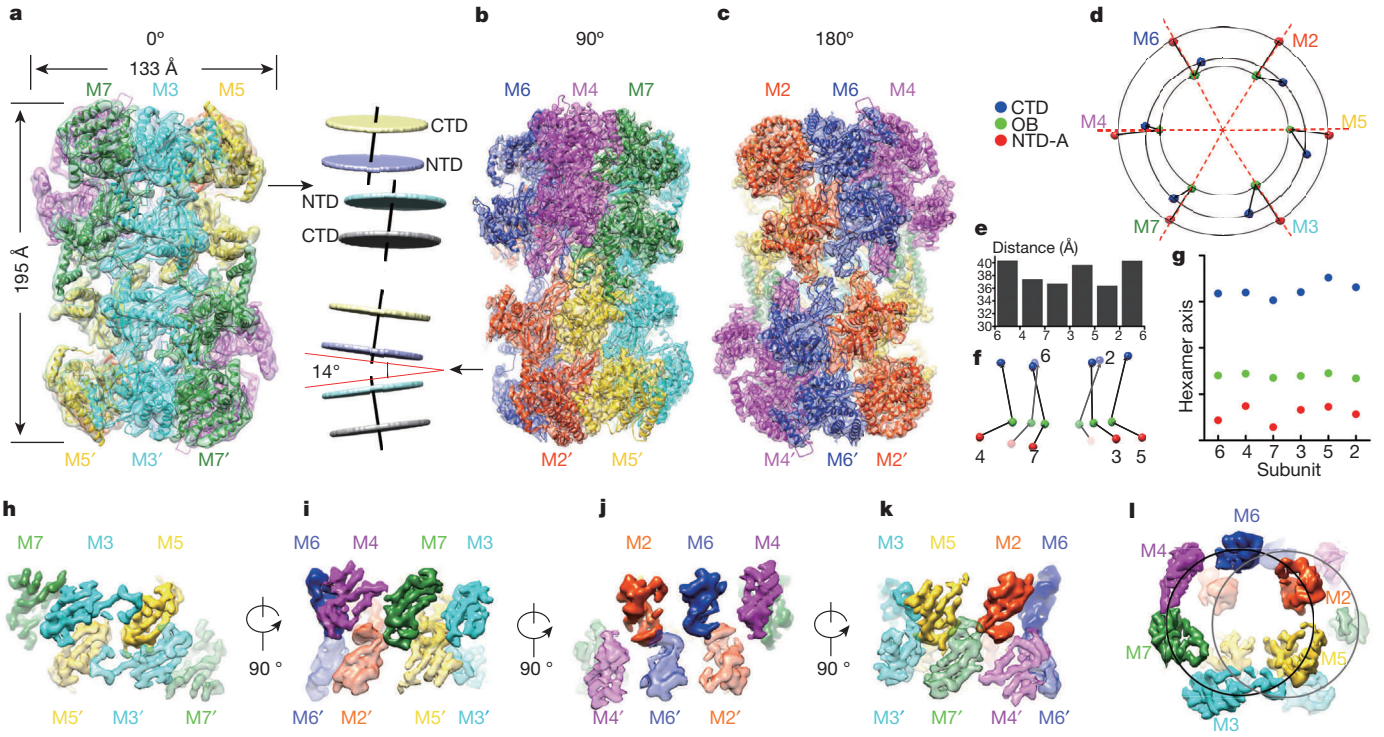

Figure 1 | Overall structure and domain organization of the MCM2–7 double hexamer. **a**–**c**, Side-views of the cryo-EM density map superimposed with the atomic model. Unsharpened map (**a**) is displayed from the two-fold axis, and sharpened map (**b**, **c**) displayed with indicated rotations relative to **a** along the cylinder axis. The side panels of **a** and **b** illustrate the tilted arrangement of the two single hexamers. **d**, **f**, Top (**d**) and side (**f**) views of the organization of the indicated structural domains. Small coloured balls denote gravity centres (see Methods) of these domains. **e**, Distances between the gravity centres of adjacent CTDs. **g**, Radial projection of **f**. **h**–**l**, Side and top views of the segmented maps (sharpened) of ZFs at the hexamer interface.

previous studies[26,34,35]. Notably, consistent with sequence analysis[36] (Extended Data Fig. 2), the ZF of MCM3 is a degenerate version without zinc binding (Extended Data Fig. 3a–c). Twelve ZFs arrange into two stacked rings at the interface (Fig. 1h–l), with an apparent centre shift (Fig. 1l and Supplementary Video 1). Inter-ZF interactions are versatile, displaying completely different patterns at opposite sides of the wedged interface (Fig. 1b, subpanel). Although ZFs are more horizontally arranged at the thin 3-5-7 edge (Fig. 1h), they are nearly vertical at the thick 2-4-6 edge (Fig. 1j). ZF interactions are largely from their polar residues, dominated by two pairs of ZF5:ZF3′ (Fig. 1h) and two pairs of ZF6:ZF2′ (Fig. 1j), as measured in buried surfaces (Extended Data Table 1a). Different ZF orientations at the hexamer interface perfectly explain the observed tilt and twist between the two single hexamers, because this unique arrangement would enable comprehensive close contacts for both edges and leads to the stabilization of the double hexamer.

Eukaryotic MCM proteins distinguish themselves from archaeal counterparts by many subunit-specific sequence extensions at their N and C termini (NTE and CTE, respectively) and insertions within functional domains. Both MCM4 and MCM6 have a very long linker between their OBs and CTDs (Extended Data Fig. 4a), which could be the underlying basis of the observed twist between NTD and CTD rings in the single hexamer (Fig. 1d). Notably, many sequence insertions and extensions also markedly contribute to the double hexamer stabilization (Fig. 2). For example, an insertion located on the β-turn of the OB from MCM6 (Extended Data Fig. 4h) interacts with the ZF of MCM2 on the other hexamer (Fig. 2e). The most unique inter-hexamer interactions involve MCM3, MCM5 and MCM7. Compared with archaeal MCMs, they have longer sequences at their N termini (Extended Data Fig. 2), which form extended strands or loops (Extended Data Fig. 4e, g and i). MCM7 also has a long insertion (~70 residues) at its NTD-A (N-terminal insertion (NTI)) (Extended Data Fig. 4a), folding into a helix–turn–helix motif (Extended Data Fig. 4i). The N terminus of MCM5 extends into the space between ZFs of MCM3 and MCM7 from the other hexamer, and forms interactions with β-strands of both ZFs (Fig. 2f and Supplementary Video 2). Furthermore, the long NTI of MCM7 extends towards the opposite MCM5 and interacts with its NTD-A (Fig. 2c, g). The N terminus of MCM7 also interacts with the N terminus of MCM3 from the other hexamer (Fig. 2h). On the basis of the calculated buried surfaces for the above interfaces (Fig. 2e–h), the contribution of NTIs and NTEs to the double hexamer stability is even greater than the ZF interactions (Extended Data Table 1a). Importantly, most insertions and extensions involved in inter-hexamer stabilization (Fig. 2) are conserved in higher eukaryotes, suggesting a universal importance of these eukaryotic-specific sequences.

MCM2, 4 and 6 have very long NTEs, which are targets of cellular signalling kinases[7–9,11]. These NTEs are highly disordered in our structure, and their involvement in inter-hexamer interaction is unknown.

Intersubunit interaction

The intersubunit interactions are very similar, and can be categorized into three tiers based on their axial locations (Extended Data Fig. 5a–c). The first one is between two contacting CTDs (ATPase domains), largely composed of hydrophobic interactions, as exemplified by a tight stacking between two surface-exposed helices from two respective CTDs (Extended Data Fig. 5a). The second tier, on the neck region of the hexamer, involves four conserved hairpins or loops from two adjacent subunits, including allosteric communication loop (ACL) and helix-2-insert (H2I) of the first subunit, and H2I and presensor 1 β-hairpin (PS1-HP) of the flanking second subunit (Extended Data Fig. 5b). Atomic interactions at the neck interfaces are versatile, involving different residues from these loops. However, a large proportion of them are polar residues, indicating electrostatic or hydrogen-bonding interactions dominate these interfaces. The third tier, contributed by the ZF of one subunit and two loops from the OB of

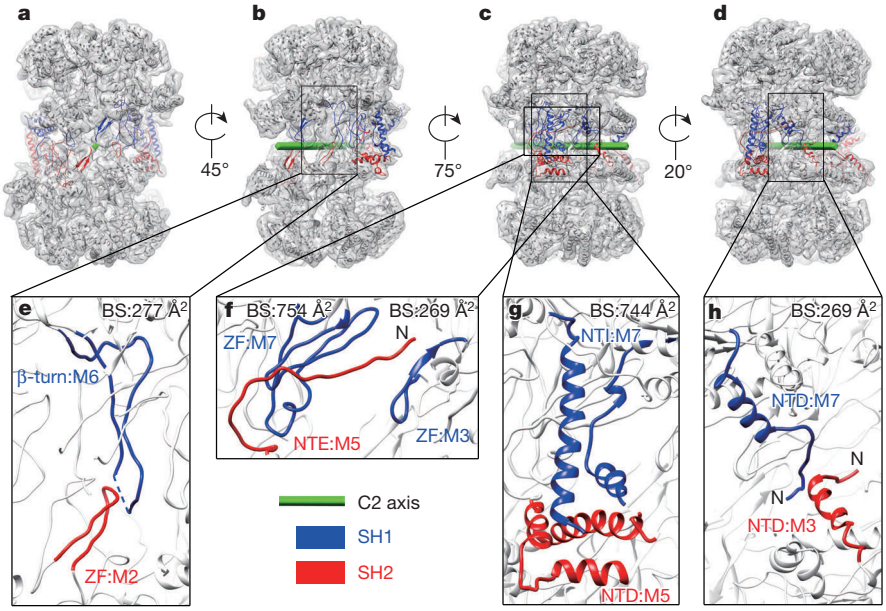

Figure 2 | Inter-hexamer interactions contributed by NTEs and NTIs. a–d, Side views of the MCM2–7 double hexamer, with indicated rotations around the cylinder axis. Atomic structure is superimposed with the unsharpened map. The sequence elements involved in inter-hexamer interactions are highlighted in blue and red representing single hexamer 1 (SH1) and SH2, respectively. **e–h**, Zoomed-in views of the boxed regions from **b–d**. Buried areas (Å^2) of these interfaces in **e–h** are labelled. BS, buried surface.

a flanking subunit (Extended Data Fig. 5c), is largely composed of hydrophobic interactions between respective β-strands or loops (for example, see Extended Data Fig. 6d). Perturbation of this interface by an MCM4 mutation (Phe391Ile) causes pre-replicative complex assembly defects in yeast and mammary carcinoma in mouse[37]. In addition, a mutation on MCM5 NTD-A (Phe83Leu) that results in Dbf4-dependent kinase (DDK)-independent activation[38] is close to this interface.

Intersubunit interactions are further enhanced by the NTIs of MCM3, 5, 6 and 7, which contact the NTD-As of their neighbouring MCM7, 3, 2 and 4, respectively (Extended Data Fig. 5d–i). Compared with other pairs, the interface of MCM5–MCM2 is without NTI involvement, a feature that may facilitate the gap opening observed between them during hexamer loading and activation[16,19–21]. At lower contour levels, four CTEs containing the winged-helix DNA binding motif could be identified for MCM4, 5, 6 and 7 (Extended Data Fig. 3d, e). The flexibility of these winged-helix-containing CTEs suggests that they are not involved in intersubunit interaction, contrasting the role of winged-helix motifs in the origin recognition complex structure[39].

The buried surfaces of the six subunit interfaces are sharply different (Extended Data Table 1a), with the smallest at 2:6, rather than at the gate-forming 2:5 interface. The weak 2:6 interface gives rise to a unique side channel (13 Å), enough to accommodate single-stranded DNA (ssDNA) (Extended Data Fig. 7 and Supplementary Video 1), in contrast to archaeal MCM structure with six side channels[23]. A ssDNA extrusion model has been proposed for the function of side channels in DNA unwinding[23,35,36]. However, unwinding studies[13–15,17] generally conflict with this model. A definitive function for this unique 2:6 side channel remains to be examined.

ATPase active centres

Remarkable conformational differences lie at the six ATPase centres of the CTD ring. Comparisons of them indicate that two active centres, 2:6 and 5:2, are apparent outliers. Their ATP-binding pockets are less compact, with sensor elements (sensors 2 and 3, and arginine finger) in MCM2 and MCM6, respectively, considerably shifted away from nucleotides, and the displacements are as large as 4–5 Å measured by Cα atoms of sensor 3 residues (Fig. 3a, b). Further analysis was done by comparisons of representative centres from the compact and loose groups with an active ATPase centre from papillomavirus E1 crystal structure[40] or an inactive one from an archaeal MCM structure[30]. Indeed, while the conformational differences of the four compact centres relative to that of E1 are small (for example, dimers of 7:3 and 4:7; Extended Data Fig. 8h, i), the loose ones display sharp differences from that of E1 (Fig. 3c, d). Moreover, the nucleotide occupancies at the centres of 3:5 and 6:4 dimers are comparatively low (Extended Data Fig. 9), consistent with their reported nearly null ATPase activities[33]. On the basis of the active centre arrangement and nucleotide occupancy, it appears that only dimers of 7:3 and 4:7 are active. This observation agrees with the extremely low ATPase activity observed in MCM2–7 as a double hexamer[18], and the reported activity of 7:3 dimer comparable to that of the whole MCM2–7 complex[33].

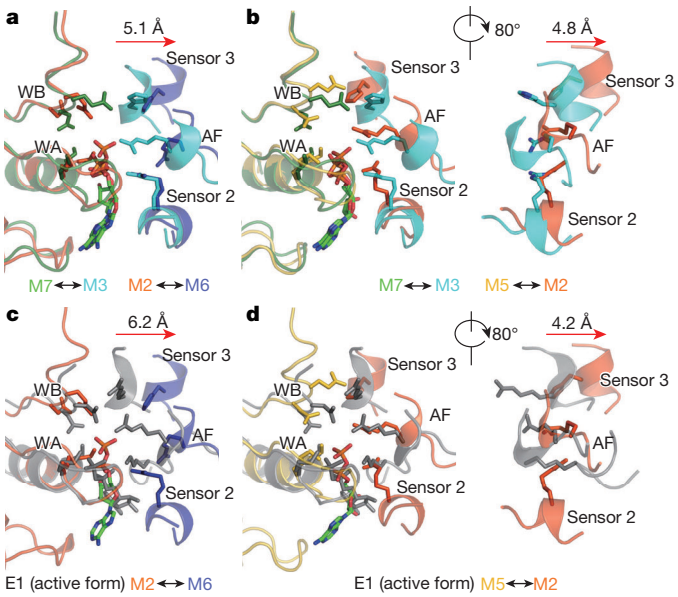

Figure 3 | Inactive ATPase centres of 2:6 and 5:2 dimers. a, b, Comparison of the ATP-binding pockets from 2:6 and 5:2 dimers with that from 7:3 dimer. Dimers (*cis*:*trans*) are presented with *cis* and *trans* ATPase elements on the left and right, respectively. **c, d**, Same as **a** and **b**, but the ATPase centres of 2:6 and 5:2 dimers are compared with that of the hexameric E1 helicase[40]. Motifs of Walker A (WA), Walker B (WB), arginine finger (AF), sensor 2 and sensor 3 are displayed in stick model. The directions and distances of sensor 3 movements are marked. All alignments were done using the Walker A and B motifs as a reference.

Previously, individual active centres were proposed to have distinct roles in regulating helicase activities[36,41,42]. Supported by our data, allosteric regulation of these ATPase centres orchestrated by the orientation changes between adjacent CTDs, might be the basis for factor-dependent control of helicase activities during different replication stages.

Axial displacement of interior hairpin loops

As in many hexameric AAA+ machineries, the central-pored chamber of MCM2–7 complex is decorated with layers of hairpin loops. For archaeal MCM, four layers of conserved loops essential for DNA binding and/or unwinding have been described[35,43], with two of them located innermost (Fig. 4a). The first one, composed of six H2Is, was previously shown to undergo axial movement depending on the nucleotide-binding states of the ATPase domains[44]. The other, composed of β-turn motifs of the six OBs, was shown to coordinate the binding of ssDNA to the MCM–ssDNA binding motifs on the channel surface of OBs in the crystal structure of an archaeal MCM NTD homohexamer[27]. In the MCM2–7 complex, these two layers of loops are placed in axially staggered positions (Fig. 4b, c), and particularly, six H2Is roughly display a helical trajectory (Fig. 4c). An alignment with the ssDNA-bound archaeal MCM hexamer[27] precisely placed ssDNA between these two layers of loops (Fig. 4b, c). In addition, when a double-stranded DNA (dsDNA) is placed in the channel, the H2Is show very close contact with it, capable of inserting their terminal loops into its major or minor grooves consecutively (Fig. 4d). At a very low threshold, an extra piece of fragmented density, which might be the residual dsDNA, could be identified within the channel at the H2I ring, but its sub-stoichiometric occupancy prevented positive identification and further analysis. Nevertheless, the snug fitting of the helically arranged H2Is and dsDNA suggests that H2I might be involved in the initial melting of origin DNA. These observations, together with repeated reports of the axial displacement of interior loops of AAA+ hexameric machines[40,45], suggest that the MCM2–7 complex uses a conserved mechanism involving cycles of ATP binding and hydrolysis to control the axial positions of the interior loops to facilitate DNA translocation and unwinding.

Central channel and model of initial origin melting

The diameter of the central channel in MCM2–7 single hexamer is not uniform (Fig. 5a, b), about 30 Å at the C-terminal end and 40 Å at the N-terminal end, but with two constriction sites (~25 Å) at H2Is and β-turn motifs that are just wide enough to accommodate dsDNA (Fig. 5c, d). However, owing to the twisted stacking between two ZF rings in the double hexamer (Fig. 5f), the channel is partially blocked at the hexamer interface by the ZF rings, splitting the wide channel at the double hexamer interface into a main central channel and two minor channels (Fig. 5f and Supplementary Video 1). The overlapping central channel is just about the size of dsDNA (Fig. 5f, g), while the minor channels are not wide enough for the passage of dsDNA (Fig. 5h) but accessible from the outside. Notably, gate-forming subunits MCM2 and MCM5 participate in the formation of both channels. The overlapping central channel is delineated by ZFs from two MCM2–MCM5 dimers and a vertically arranged MCM6 dimer (Fig. 5g), and the minor channel involves ZFs from MCM2 and 5 of one single hexamer, and MCM3 and 7 of the other single hexamer (Fig. 5h).

The structure of an already constricted central channel of the single hexamer that opens to a larger channel at the NTD only to be occluded by the offset of the ZF rings at the double hexamer interface invites

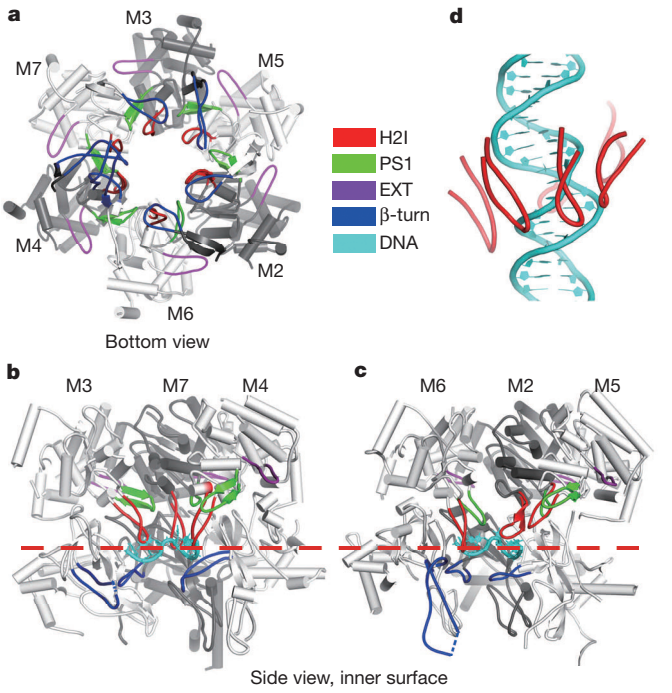

Figure 4 | Spatial distribution of conserved hairpins in the single hexamer. **a**, Bottom view (from the hexamer interface) of the MCM2–7 hexamer. The six MCM subunits are shown in alternating grey scales, with four hairpins highlighted in indicated colours. All four hairpins are at the subunit interface, and extend towards the adjacent subunit. **b**, **c**, Side views of the inner surface of the hexamer, docked with a model ssDNA from an archaeal MCM structure (PDB accession code 4POG)[27]. **d**, Contacts between H2Is and dsDNA illustrated through fitting a dsDNA fragment into the central channel of the hexamer.

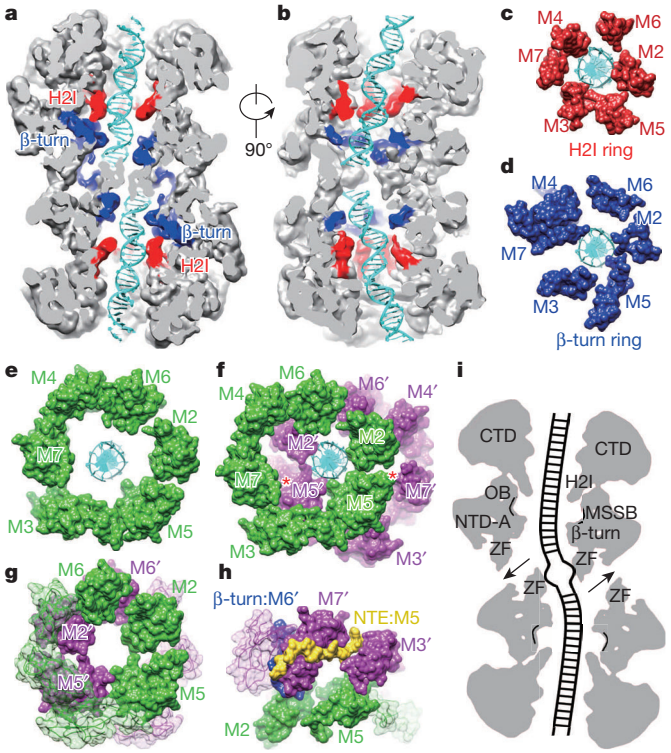

Figure 5 | Central channel and its implication in origin melting. **a**, **b**, Cut-away views of the density map (unsharpened) with two dsDNA fragments fitted in the central channel. **c**–**f**, Surface representation (top view) of the atomic models of the six H2Is (**c**), β-turns (**d**), ZFs (**e**) from one single hexamer, and ZFs from both single hexamers (**f**). Red asterisks mark the positions of two minor channels. **g**, **h**, Double hexamer interface centred for the views of the narrowed central channel (**g**), and minor channel (**h**). ZFs not part of the constricted central channel are in high transparency. **i**, Model for initial origin melting (see text).

speculations for functions. First, the kink in the central channel created by the offset of the two single hexamer rings will probably cause deformation of trapped duplex DNA (Fig. 5i) to create a nucleation centre for DNA melting. Second, the tight grip of the duplex DNA on either ends by the helically positioned H2Is serves to hold the kinked DNA in place such that a slight left-handed rotation between the two single hexamers, as previously proposed[18], could further deform the origin DNA at the nucleation point. Third, possible relative rotation between the NTD and CTD rings within single hexamers upon helicase activation, might further lower the activation energy of DNA melting. We envision that initial melting involves allosteric conformational changes, in combination with dsDNA translocation in opposite directions by the coupled single hexamers[32]. The dsDNA being pumped into the central channel provides the slack necessary for strand separation. This initial melting step requires the activation of the MCM2–7 helicase activity most likely by DDK phosphorylation and binding of Cdc45 and GINS[12]. Recent studies showed that DDK phosphorylation of the NTEs of MCM2–7 does not cause double hexamer separation[18,46], but promotes MCM2–MCM5 gate opening[47]. Opening of the MCM2–MCM5 gates at this point would merge central and minor channels, creating an expanded N-terminal chamber for strand separation. The ssDNA looping out through this chamber would be accessible to replication factors lurking nearby (Fig. 5i). Further strand separation towards the CTD ring may be facilitated by the interior β-hairpin loops and the MCM–ssDNA binding motifs[27] on the inner surface of OBs.

This structure-informed hypothesis on the initial origin melting is in accordance with previous data. First, many factors required for helicase activation, such as Sld2, Sld3, Cdc45 and Mcm10, have well-defined ssDNA binding activity[11,16,32,48–50]. Second, a similar replicative helicase SV40 large tumour antigen initiates origin melting as a dsDNA pump[32,35], and conformational rearrangements of the two single hexamers were observed during this process[31]. Our structure suggests that, in addition to its role in processive fork unwinding, MCM2–7 is also actively involved in origin DNA melting. In transitioning from the initial origin melting state to the fork unwinding state, MCM2–7 essentially translocates first on dsDNA (dsDNA pump) and then along ssDNA (steric exclusion).

In summary, the fine structural details provided in this work will serve as a rich source of information for designing and interpreting biochemical studies aimed at dissecting the mechanistic functions of the MCM2–7 complex. In particular, it will provide a framework for future study of the eukaryotic-specific assembly, activation and regulation of this helicase family.

Online Content Methods, along with any additional Extended Data display items and Source Data, are available in the online version of the paper; references unique to these sections appear only in the online paper.

Received 25 March 2015; accepted 25 June 2015.

Published online 29 July 2015.

1. O'Donnell, M., Langston, L. & Stillman, B. Principles and concepts of DNA replication in bacteria, archaea, and eukarya. *Cold Spring Harb. Perspect. Biol.* **5,** a010108 (2013).
2. Costa, A., Hood, I. V. & Berger, J. M. Mechanisms for initiating cellular DNA replication. *Annu. Rev. Biochem.* **82,** 25–54 (2013).
3. Duderstadt, K. E. & Berger, J. M. A structural framework for replication origin opening by AAA+ initiation factors. *Curr. Opin. Struct. Biol.* **23,** 144–153 (2013).
4. Tye, B. K. MCM proteins in DNA replication. *Annu. Rev. Biochem.* **68,** 649–686 (1999).
5. Remus, D. *et al.* Concerted loading of Mcm2–7 double hexamers around DNA during DNA replication origin licensing. *Cell* **139,** 719–730 (2009).
6. Evrin, C. *et al.* A double-hexameric MCM2–7 complex is loaded onto origin DNA during licensing of eukaryotic DNA replication. *Proc. Natl Acad. Sci. USA* **106,** 20240–20245 (2009).
7. Siddiqui, K., On, K. F. & Diffley, J. F. Regulating DNA replication in eukarya. *Cold Spring Harb. Perspect. Biol.* **5,** a012930 (2013).
8. Heller, R. C. *et al.* Eukaryotic origin-dependent DNA replication *in vitro* reveals sequential action of DDK and S-CDK kinases. *Cell* **146,** 80–91 (2011).
9. Yeeles, J. T., Deegan, T. D., Janska, A., Early, A. & Diffley, J. F. Regulated eukaryotic DNA replication origin firing with purified proteins. *Nature* **519,** 431–435 (2015).
10. Tanaka, S. & Araki, H. Helicase activation and establishment of replication forks at chromosomal origins of replication. *Cold Spring Harb. Perspect. Biol.* **5,** a01037 (2013).
11. Tognetti, S., Riera, A. & Speck, C. Switch on the engine: how the eukaryotic replicative helicase MCM2–7 becomes activated. *Chromosoma* **124,** 13–26 (2015).
12. Ilves, I., Petojevic, T., Pesavento, J. J. & Botchan, M. R. Activation of the MCM2–7 helicase by association with Cdc45 and GINS proteins. *Mol. Cell* **37,** 247–258 (2010).
13. Fu, Y. V. *et al.* Selective bypass of a lagging strand roadblock by the eukaryotic replicative DNA helicase. *Cell* **146,** 931–941 (2011).
14. Rothenberg, E., Trakselis, M. A., Bell, S. D. & Ha, T. MCM forked substrate specificity involves dynamic interaction with the 5′-tail. *J. Biol. Chem.* **282,** 34229–34234 (2007).
15. McGeoch, A. T., Trakselis, M. A., Laskey, R. A. & Bell, S. D. Organization of the archaeal MCM complex on DNA and implications for the helicase mechanism. *Nature Struct. Mol. Biol.* **12,** 756–762 (2005).
16. Costa, A. *et al.* DNA binding polarity, dimerization, and ATPase ring remodeling in the CMG helicase of the eukaryotic replisome. *eLife* **3,** e03273 (2014).
17. Graham, B. W., Schauer, G. D., Leuba, S. H. & Trakselis, M. A. Steric exclusion and wrapping of the excluded DNA strand occurs along discrete external binding paths during MCM helicase unwinding. *Nucleic Acids Res.* **39,** 6585–6595 (2011).
18. Sun, J. *et al.* Structural and mechanistic insights into Mcm2–7 double-hexamer assembly and function. *Genes Dev.* **28,** 2291–2303 (2014).
19. Samel, S. A. *et al.* A unique DNA entry gate serves for regulated loading of the eukaryotic replicative helicase MCM2–7 onto DNA. *Genes Dev.* **28,** 1653–1666 (2014).
20. Sun, J. *et al.* Cryo-EM structure of a helicase loading intermediate containing ORC-Cdc6-Cdt1–MCM2–7 bound to DNA. *Nature Struct. Mol. Biol.* **20,** 944–951 (2013).
21. Costa, A. *et al.* The structural basis for MCM2–7 helicase activation by GINS and Cdc45. *Nature Struct. Mol. Biol.* **18,** 471–477 (2011).
22. Hesketh, E. L. *et al.* DNA induces conformational changes in a recombinant human minichromosome maintenance complex. *J. Biol. Chem.* **290,** 7973–7979 (2015).
23. Brewster, A. S. *et al.* Crystal structure of a near-full-length archaeal MCM: functional insights for an AAA+ hexameric helicase. *Proc. Natl Acad. Sci. USA* **105,** 20191–20196 (2008).
24. Bae, B. *et al.* Insights into the architecture of the replicative helicase from the structure of an archaeal MCM homolog. *Structure* **17,** 211–222 (2009).
25. Slaymaker, I. M. *et al.* Mini-chromosome maintenance complexes form a filament to remodel DNA structure and topology. *Nucleic Acids Res.* **41,** 3446–3456 (2013).
26. Fletcher, R. J. *et al.* The structure and function of MCM from archaeal *M. thermoautotrophicum*. *Nature Struct. Biol.* **10,** 160–167 (2003).
27. Froelich, C. A., Kang, S., Epling, L. B., Bell, S. P. & Enemark, E. J. A conserved MCM single-stranded DNA binding element is essential for replication initiation. *eLife* **3,** e01993 (2014).
28. Fu, Y., Slaymaker, I. M., Wang, J., Wang, G. & Chen, X. S. The 1.8-Å crystal structure of the N-terminal domain of an archaeal MCM as a right-handed filament. *J. Mol. Biol.* **426,** 1512–1523 (2014).
29. Liu, W., Pucci, B., Rossi, M., Pisani, F. M. & Ladenstein, R. Structural analysis of the *Sulfolobus solfataricus* MCM protein N-terminal domain. *Nucleic Acids Res.* **36,** 3235–3243 (2008).
30. Miller, J. M., Arachea, B. T., Epling, L. B. & Enemark, E. J. Analysis of the crystal structure of an active MCM hexamer. *eLife* **3,** e03433 (2014).
31. Cuesta, I. *et al.* Conformational rearrangements of SV40 large T antigen during early replication events. *J. Mol. Biol.* **397,** 1276–1286 (2010).
32. Vijayraghavan, S. & Schwacha, A. The eukaryotic Mcm2–7 replicative helicase. *Subcell. Biochem.* **62,** 113–134 (2012).
33. Bochman, M. L., Bell, S. P. & Schwacha, A. Subunit organization of Mcm2–7 and the unequal role of active sites in ATP hydrolysis and viability. *Mol. Cell. Biol.* **28,** 5865–5873 (2008).
34. Evrin, C. *et al.* The ORC/Cdc6/MCM2–7 complex facilitates MCM2–7 dimerization during prereplicative complex formation. *Nucleic Acids Res.* **42,** 2257–2269 (2014).
35. Slaymaker, I. M. & Chen, X. S. MCM structure and mechanics: what we have learned from archaeal MCM. *Subcell. Biochem.* **62,** 89–111 (2012).
36. Bochman, M. L. & Schwacha, A. The Mcm complex: unwinding the mechanism of a replicative helicase. *Microbiol. Mol. Biol. Rev.* **73,** 652–683 (2009).
37. Shima, N. *et al.* A viable allele of Mcm4 causes chromosome instability and mammary adenocarcinomas in mice. *Nature Genet.* **39,** 93–98 (2007).
38. Hardy, C. F., Dryga, O., Seematter, S., Pahl, P. M. & Sclafani, R. A. mcm5/cdc46-bob1 bypasses the requirement for the S phase activator Cdc7p. *Proc. Natl Acad. Sci. USA* **94,** 3151–3155 (1997).
39. Bleichert, F., Botchan, M. R. & Berger, J. M. Crystal structure of the eukaryotic origin recognition complex. *Nature* **519,** 321–326 (2015).
40. Enemark, E. J. & Joshua-Tor, L. Mechanism of DNA translocation in a replicative hexameric helicase. *Nature* **442,** 270–275 (2006).
41. Kang, S., Warner, M. D. & Bell, S. P. Multiple functions for Mcm2–7 ATPase motifs during replication initiation. *Mol. Cell* **55,** 655–665 (2014).
42. Coster, G., Frigola, J., Beuron, F., Morris, E. P. & Diffley, J. F. Origin licensing requires ATP binding and hydrolysis by the MCM replicative helicase. *Mol. Cell* **55,** 666–677 (2014).
43. Bell, S. D. & Botchan, M. R. The minichromosome maintenance replicative helicase. *Cold Spring Harb. Perspect. Biol.* **5,** a012807 (2013).
44. Jenkinson, E. R. & Chong, J. P. Minichromosome maintenance helicase activity is controlled by N- and C-terminal motifs and requires the ATPase domain helix-2 insert. *Proc. Natl Acad. Sci. USA* **103,** 7613–7618 (2006).

45. Gai, D., Zhao, R., Li, D., Finkielstein, C. V. & Chen, X. S. Mechanisms of conformational change for a replicative hexameric helicase of SV40 large tumor antigen. *Cell* **119,** 47–60 (2004).
46. On, K. F. *et al.* Prereplicative complexes assembled *in vitro* support origin-dependent and independent DNA replication. *EMBO J.* **33,** 605–620 (2014).
47. Bruck, I. & Kaplan, D. L. The Dbf4-Cdc7 kinase promotes Mcm2–7 ring opening to allow for single-stranded DNA extrusion and helicase assembly. *J. Biol. Chem.* **290,** 1210–1221 (2015).
48. Bruck, I. & Kaplan, D. L. Cdc45 protein-single-stranded DNA interaction is important for stalling the helicase during replication stress. *J. Biol. Chem.* **288,** 7550–7563 (2013).
49. Fien, K. *et al.* Primer utilization by DNA polymerase α-primase is influenced by its interaction with Mcm10p. *J. Biol. Chem.* **279,** 16144–16153 (2004).
50. Eisenberg, S., Korza, G., Carson, J., Liachko, I. & Tye, B. K. Novel DNA binding properties of the Mcm10 protein from *Saccharomyces cerevisiae*. *J. Biol. Chem.* **284,** 25412–25420 (2009).

Supplementary Information is available in the online version of the paper.

Acknowledgements We thank X. Li for providing programs in data collection, motion correction and framed-based analysis, and J. Wang for advices on modelling and model refinement. We also thank the National Center for Protein Sciences (Beijing, China) for technical support with cryo-EM data collection and for computation resource. This work was supported by the Ministry of Science and Technology of China (2013CB910404 to N.G.), the National Natural Science Foundation of China (31422016 to N.G.), the Research Grants Council of Hong Kong (GRF664013 and HKUST12/CRF/13G to Yu.Z.) and the Hong Kong University of Science & Technology (B.-K.T.).

Author Contributions Yu.Z. purified sample; N.L. collected cryo-EM data (with J.L., Yi.Z. and W.L), performed image processing, and analyzed structures. N.L., N.G. and M.Y. performed atomic modelling. N.L., Yu.Z., B.-K.T. and N.G. designed experiments, interpreted the structure and wrote the manuscript.

Author Information The cryo-EM density map has been deposited in the Electron Microscopy Data Bank (EMDB) under accession number EMD-6338; and the atomic model has been deposited in the Protein Data Bank (PDB) under accession number 3JA8. Reprints and permissions information is available at www.nature.com/reprints. The authors declare no competing financial interests. Readers are welcome to comment on the online version of the paper. Correspondence and requests for materials should be addressed to N.G. (ninggao@tsinghua.edu.cn), B.-K.T. (bt16@cornell.edu), or Yu.Z. (zhai@ust.hk).

METHODS

No statistical methods were used to predetermine sample size.

Yeast strain. One-step PCR-based approach[51] with pTF272 (pFA6a-TEV-6×Gly-3×Flag-HphMX, Addgene) as DNA template was used to generate MCM4-TEV-3×Flag tagging modification in the W303-1a background strain. The resulting strain showed no growth defect compared to its parent W303-1a strain.

Sample purification. Forty litres of log-phase G1 yeast cells (3×10^7–4×10^7 cells per ml) were collected and processed for spheroplasting to isolate crude chromatin as described previously[52] with the following modifications for a large-scale preparation. Spheroplasting was performed in 200 ml of spheroplasting buffer containing sufficient amount of lyticase that was purified from an *Escherichia coli* strain bearing lyticase expressing plasmid pUV5-G1S (gift from S. Gasser). The spheroplasts were lysed with extraction buffer EBX (50 mM HEPES/KOH, pH 7.5, 100 mM K-glutamate, 10 mM magnesium acetate, 0.25% Triton X-100, 3 mM ATP, 1 mM dithiothreitol (DTT), 1 mM EDTA, 2 mM NaF, 1 mM $NaVO_4$, 1 mM phenylmethanesulfonylfluoride (PMSF), 2 μg ml^{-1} pepstatin A and 1× protease inhibitor cocktail (Roche)). The lysate was layered onto the top of equal volume of EBX buffer containing 30% sucrose and centrifuged at 25,000*g* (Hitachi R20A2) for 15 min. To solubilize chromatin fractions, the crude chromatin was digested in 40 ml of freshly made benzonase buffer (50 mM HEPES/KOH, pH 7.5, 100 mM K-glutamate, 8 mM $MgCl_2$, 0.02% NP-40, 3 mM ATP, 1 mM EDTA, 2 mM NaF, 1 mM $NaVO_4$, 1 mM PMSF, 2 μg ml^{-1} pepstatin A and 1× protease inhibitor cocktail (Roche)) with 1 U μl^{-1} of benzonase (71206-3; Merck Biosciences) for 10 min at 37 °C, and then 1 h on ice. The suspension was then centrifuged for 20 min at 25,000*g*. The clear phase was recovered, and subjected to anti-Flag immunoprecipitation with 1 ml bed volume of washed anti-Flag M2 agarose (Sigma) at 4 °C for 2 h. Beads were recovered, and washed extensively with benzonase buffer and then tobacco etch virus (TEV) buffer (50 mM HEPES/KOH, pH 7.5, 100 mM K-glutamate, 8mM $MgCl_2$, 0.02% NP-40, 3 mM ATP). MCM2–7 complexes were cleaved from the M2 agarose by incubation for overnight at 4 °C in TEV buffer with 100 U ml^{-1} of AcTEV protease (Life Technology). His-tagged TEV protease was removed by incubating the eluate with a TALON metal affinity resin (Clontech) for 30 min at 4 °C. The MCM2–7 complexes were then applied on the top of 20–40% glycerol gradient in buffer EBX with protease inhibitors. The glycerol gradient was centrifuged in a TLS-55 rotor (Beckman Optima TLX ultracentrifuge) at 175,000*g* for 6.5 h. The fractions were collected from the top of the gradient after centrifugation. The fractions containing the MCM2–7 double hexamers were pooled and processed for electron microscopy analysis.

Electron microscopy. The MCM2–7 double hexamer was concentrated by ultrafiltration to remove glycerol. Negative staining of the MCM2–7 double hexamer was performed with 2% uranyl acetate. Grids were examined using an FEI T12 microscope operated at 120 kV, and images were recorded using a 4k × 4k charge-coupled device (CCD) camera (UltraScan 4000, Gatan).

For cryo-grid preparation, 4 μl aliquots of samples were applied to a glow-discharged holy carbon grid (Quantifoil R2/2) coated with a thin layer of freshly prepared carbon, and cryo-freezing was performed with an FEI Vitrobot Mark IV (4 °C and 100% humidity). Grids were examined using an FEI Titan Krios operated at 300 kV, and images were recorded using a K2 Summit direct electron detector (Gatan) in counting mode, at a nominal magnification of 22,500×, which renders a final pixel size of 1.32 Å at object scale after post-magnification calibration, and with the defocus ranging from −1.5 to −2.5 μm. Images were collected under low-dose condition in a semi-automatic manner using UCSF-Image4 (written by X. Li and Y. Cheng). For each micrograph stack, a total of 32 frames were collected, with a dose rate of ~8.2 counts (~10.9 electrons) per physical pixel per second for an exposure time of 8 s.

Image processing. Initial 3D model from negatively stained particles was calculated using RELION[53] using a density cylinder as reference. For cryo-EM data, beam-induced motion correction at micrograph level was performed as previously described (written by X. Li)[54]. Micrographs screening, automatic particle picking and normalization were done with SPIDER[55]. Program of CTFFIND3 (ref. 56) was used to estimate the contrast transfer function parameters. The 2D, 3D classification and refinement were performed with RELION. A total of 347,801 particles (with a binning factor of two) from 2,230 micrographs were subjected to a cascade of 2D and 3D classification. Analysis of classification structures indicated that there is a C2-axis perpendicular to the cylinder axis of the MCM2–7 double hexamer, reflecting a symmetric arrangement of one single hexamer relatively to the other single hexamer by a simple 180° rotation. A final structurally homogeneous data set composed of 85,365 particles, as classification structures of them have reached to considerably higher resolution, in full window size (300 × 300) were used for high-resolution refinement with C2-symmetry imposed. From the orientation distribution (Extended Data Fig. 1h, i), there is a wide equator belt with a complete distribution of particles, along with two regions with relatively more particles. Nevertheless, this type of uneven distribution did not affect our final reconstruction, as particles from the equator belt have provided sufficient information for a complete sampling of the central slices in the Fourier space. Symmetry-free refinement was also performed, resulting in generally similar but slightly worse density maps. To improve the resolution further, different combinations of movie frames were used for motion correction and frame averaging. The first two frames had large motions, therefore, frames 3–16 were used to sum micrographs. To reduce interpolation errors, particles were rewindowed by offsetting translation parameters determined in the 3D refinement of last round, which improved the resolution to 4.6 Å (gold-standard FSC 0.143 criteria). The final round of refinement was performed with a soft-edged mask applied, resulting in a 4.3-Å map. After correction for the modulation transfer function of K2 detector, and map sharpening using post-processing options of RELION with a B-factor of -100 $Å^2$, the overall resolution of the final density map within the region defined by the soft mask is 3.8 Å for the overall map (Extended Data Fig. 1k), after correction of the effect of soft mask on the FSC curve[57]. Local resolution map was estimated using *blocres* in Bsoft[58]. From the local resolution map, peripheral regions are associated with worst resolution, while the core region is better than 3.5 Å. The statistics of the data collection and structural refinement is provided in Extended Data Table 1b.

Model building. Six monomers of the crystal structure of a chimaeric archaeal MCM (PDB code 4R7Y)[30] (*Sulfolobus solfataricus* NTD fused with *Pyrococcus furiosus* CTD) hexamer were manually docked to the density map of the MCM double hexamer using Chimera[59]. The docking also confirmed the handedness of the density map. The rigid-body docking was performed by dividing the crystal structure of the monomer into four pieces (NTD-A, OB-fold, ZF and CTD) (Extended Data Fig. 4b, c). Sequence alignments of the yeast MCM proteins with crystal template were initially performed using BLAST[60] and manually adjusted according to the secondary structure prediction of these sequences (PSIPRED)[61]. The predicted secondary structural information of the eukaryotic subunit-specific sequences was used to assign the six MCM proteins into the cryo-EM density map. Initial atomic coordinates of the OB-fold subdomains and CTDs of MCM2–7 proteins were then generated using CHAINSAW[62] in the *CCP4* suite[63]. Models were manually adjusted and built in Coot[64]. Only minor changes were required for modelling the OB-fold subdomains and CTDs of the yeast MCM proteins owing to their high sequence identity to the template (Extended Data Fig. 2). The NTD-As of the yeast MCM proteins contain many sequence insertions, and the modelling of these sequences was similar to that described above, but involved multiple rounds of realignment of sequences and largely facilitated by the predicted secondary structure. In many cases, the modelling of NTD-A required complete retracing of the main-chain based solely on densities and secondary structural predictions. For regions independent of known template (eukaryotic-specific sequences, Extended Data Fig. 4), poly-alanine models were built first using Coot. Clearly resolved bulky residues (Phe, Tyr, Trp and Arg) were then used as markers to assign the primary sequences. As a result, we derived an atomic model of the MCM2–7 double hexamer, for ~80% of its sequences, from a near-atomic cryo-EM density map, integrated with structural information from other sources. Further model refinement was done by alternating rounds of model rebuilding in Coot and real-space refinement (phenix.real_space_refine)[65] in Phenix[66], with secondary structure and stereochemical constraints applied. Similar to a previous cryo-EM work with comparable 3.8-Å resolution[67], during the real-space refinement, knowledge-based restraints, including Ramachandran potentials and rotamer correction, were applied to ensure a proper balance between density-fitting and stereochemical and rotamer distributions. Owing to the resolution limitation, local densities at the ATP-binding sites could not unambiguously distinguish between ATP and ADP. For modelling purpose, ADP was docked to the active centres and similarly refined in Phenix. The atomic model was cross-validated according to previously described procedures[68,69]. Specifically, the coordinates of the final model were randomly displaced by 0.2 Å using the PDB tools of Phenix. The displaced model was refined against the Half1 map (produced from a half set of all particles during refinement by RELION). The refined model from Half1 map was compared with the maps of Half1, Half2 in Fourier space to produce two FSC curves, FSC_{work} (model versus Half1 map) and FSC_{free} (model versus Half2 map), respectively (Extended Data Fig. 1l). Another FSC curve between the refined model from Half1 and the final density map (model versus merge) from all particles was also produced. As indicated by these curves, the agreement between FSC_{work} and FSC_{free} (no large separation) indicated that the model was not overfitted. MolProbity[70] (http://molprobity.biochem.duke.edu/) was used to evaluate the final model, and final statistics of the model was provided in Extended Data Table 1b. Notably, applica-

tion of knowledge-based restraints during the real-space refinement has improved the stereochemical and rotamer statistics of the model. Comparisons of the representative density with the atomic model for selected areas are shown in Extended Data Fig. 6 and Supplementary Video 2.

Gravity centres of individual domains (Fig. 1) were determined with segmented maps of the conserved core regions of these domains (minus variable loops and linkers) using SPIDER. To determine the cylinder axis of the hexamer, a plane perpendicular to the axis was determined by least-square fitting of six centres of the OBs in Chimera. Pymol[71] and Chimera were used for structural analysis and figure preparation. Interface areas of the intersubunit and inter-hexamer interactions were calculated by PISA[72], and provided in Extended Data Table 1a.

51. Janke, C. *et al.* A versatile toolbox for PCR-based tagging of yeast genes: new fluorescent proteins, more markers and promoter substitution cassettes. *Yeast* **21,** 947–962 (2004).
52. Zhai, Y., Yung, P. Y., Huo, L. & Liang, C. Cdc14p resets the competency of replication licensing by dephosphorylating multiple initiation proteins during mitotic exit in budding yeast. *J. Cell Sci.* **123,** 3933–3943 (2010).
53. Scheres, S. H. A Bayesian view on cryo-EM structure determination. *J. Mol. Biol.* **415,** 406–418 (2012).
54. Li, X. *et al.* Electron counting and beam-induced motion correction enable near-atomic-resolution single-particle cryo-EM. *Nature Methods* **10,** 584–590 (2013).
55. Shaikh, T. R. *et al.* SPIDER image processing for single-particle reconstruction of biological macromolecules from electron micrographs. *Nature Protocols* **3,** 1941–1974 (2008).
56. Mindell, J. A. & Grigorieff, N. Accurate determination of local defocus and specimen tilt in electron microscopy. *J. Struct. Biol.* **142,** 334–347 (2003).
57. Chen, S. *et al.* High-resolution noise substitution to measure overfitting and validate resolution in 3D structure determination by single particle electron cryomicroscopy. *Ultramicroscopy* **135,** 24–35 (2013).
58. Heymann, J. B. & Belnap, D. M. Bsoft: image processing and molecular modeling for electron microscopy. *J. Struct. Biol.* **157,** 3–18 (2007).
59. Pettersen, E. F. *et al.* UCSF Chimera–a visualization system for exploratory research and analysis. *J. Comput. Chem.* **25,** 1605–1612 (2004).
60. Mount, D. W. Using the Basic Local Alignment Search Tool (BLAST). *CSH Protoc.* **2007,** pdb.top17 (2007).
61. Buchan, D. W., Minneci, F., Nugent, T. C., Bryson, K. & Jones, D. T. Scalable web services for the PSIPRED Protein Analysis Workbench. *Nucleic Acids Res.* **41,** W349–W357 (2013).
62. Stein, N. CHAINSAW: a program for mutating pdb files used as templates in molecular replacement. *J. Appl. Crystallogr.* **41,** 641–643 (2008).
63. Winn, M. D. *et al.* Overview of the *CCP*4 suite and current developments. *Acta Crystallogr. D* **67,** 235–242 (2011).
64. Emsley, P., Lohkamp, B., Scott, W. G. & Cowtan, K. Features and development of Coot. *Acta Crystallogr. D* **66,** 486–501 (2010).
65. Afonine, P. V. *et al.* Towards automated crystallographic structure refinement with phenix.refine. *Acta Crystallogr. D* **68,** 352–367 (2012).
66. Adams, P. D. *et al.* PHENIX: a comprehensive Python-based system for macromolecular structure solution. *Acta Crystallogr. D* **66,** 213–221 (2010).
67. Wang, Z. *et al.* An atomic model of brome mosaic virus using direct electron detection and real-space optimization. *Nature Commun.* **5,** 4808 (2014).
68. Zhao, M. *et al.* Mechanistic insights into the recycling machine of the SNARE complex. *Nature* **518,** 61–67 (2015).
69. Amunts, A. *et al.* Structure of the yeast mitochondrial large ribosomal subunit. *Science* **343,** 1485–1489 (2014).
70. Chen, V. B. *et al.* MolProbity: all-atom structure validation for macromolecular crystallography. *Acta Crystallogr. D* **66,** 12–21 (2010).
71. Schrodinger, L. L. C. *The PyMOL Molecular Graphics System* v.1.3r1 (2010).
72. Krissinel, E. & Henrick, K. Inference of macromolecular assemblies from crystalline state. *J. Mol. Biol.* **372,** 774–797 (2007).
73. Hall, T. A. BioEdit: a user-friendly biological sequence alignment editor and analysis program for Windows 95/98/NT. *Nucleic Acids Symposium Series* **41,** 95–98 (1999).
74. Wei, Z. *et al.* Characterization and structure determination of the Cdt1 binding domain of human minichromosome maintenance (Mcm) 6. *J. Biol. Chem.* **285,** 12469–12473 (2010).

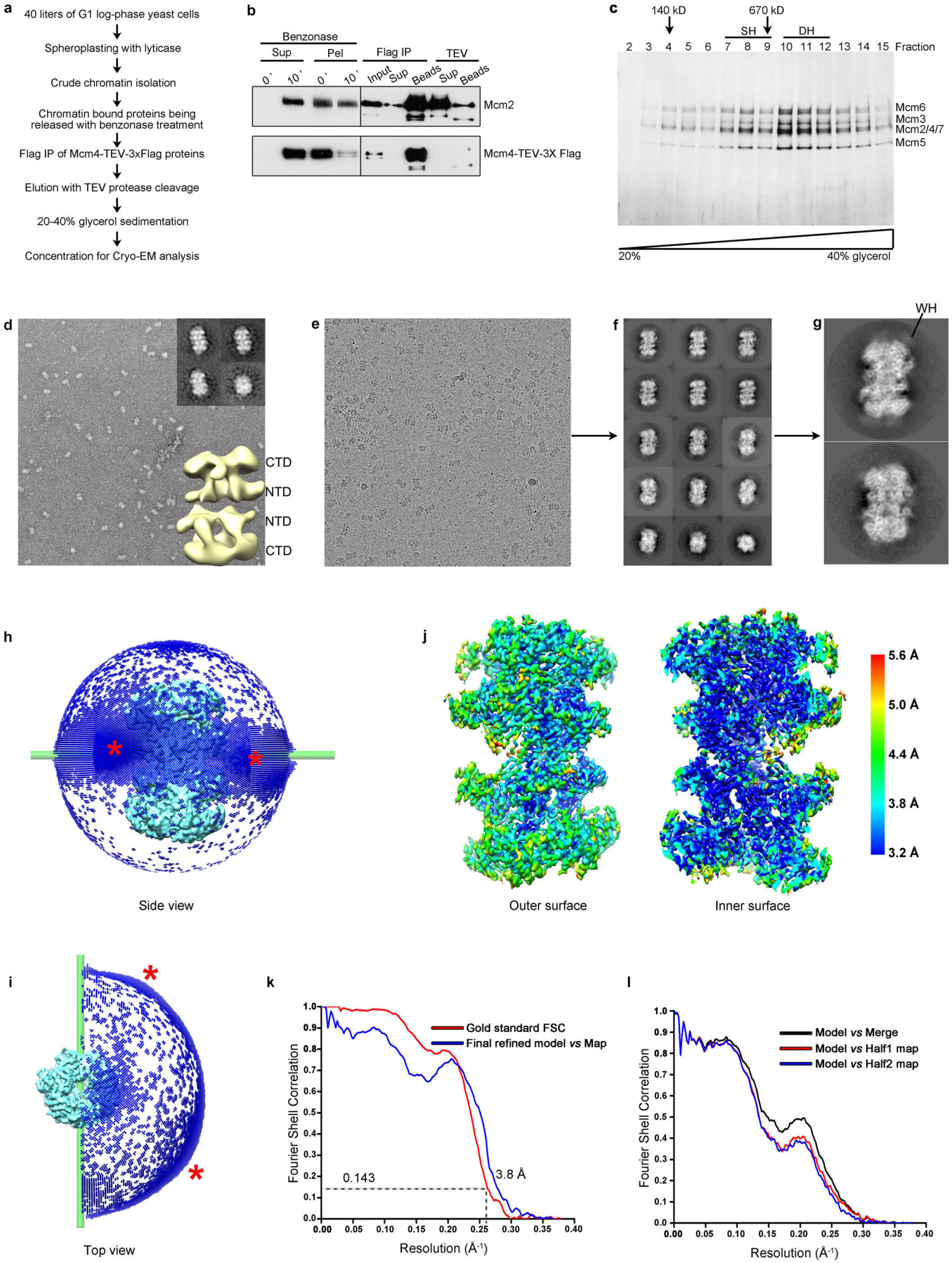

Extended Data Figure 1 | MCM2–7 double hexamer purification and structural determination. **a**, A flowchart of the procedure for MCM2–7 double hexamer purification from G1 chromatin of the yeast strain MCM4-TEV-3×Flag. **b**, Fractions taken were analysed by SDS–PAGE and immunoblotting of the indicated MCM subunits. **c**, The eluted MCM2–7 complexes were subjected to 20–40% glycerol gradient sedimentation at 175,000*g* for 6.5 h. Collected fractions were analysed by SDS–PAGE and visualized by silver staining. Molecular size markers used are: ALP 140 kDa and thyroglobulin 670 kDa. Fractions 10–12 were pooled and concentrated for cryo-EM analysis. **d**, A representative raw micrograph of the negatively stained MCM2–7 double hexamer. Representative 2D class averages of negatively stained particles produced by reference-free classification are shown at the top-right corner. The initial 3D model generated using RELION is shown at the bottom-right corner. **e**, A representative raw micrograph of cryo-EM data. **f**, Representative 2D class averages of cryo-EM particles from reference-free classification. **g**, Two typical side views of the average images from **f**, in enlarged forms, highlighting well-resolved secondary structure elements. Extra densities with poor quality on the two ends of double hexamer could be attributed to the flexible winged-helix motifs (WH) within the CTEs of MCM proteins. **h**, **i**, Distribution of particle orientations in the last round of structural refinement, showing in side (**h**) and top (**i**) views. The heights of blue cylinders at different projection directions on the surface of a hemisphere are proportional to their particle numbers. Two areas (red asterisks) of a dense equator belt are slightly enriched with particles. **j**, The density map of the MCM2–7 double hexamer (sharpened) is shown in two views, for the outer (left) and inner (right) surfaces. The map is colour-coded to indicate the range of the local resolution. **k**, Fourier shell correlation (FSC) curves for the final 3D density map after RELION-based post-processing (red, gold-standard FSC), and for the cross-examination between final atomic model and the 3D density map (blue, final refined model versus map). At a FSC 0.143 cut-off, the overall resolution for the map is 3.8 Å. **l**, FSC curves for the atomic model cross-validation. See Methods for details.

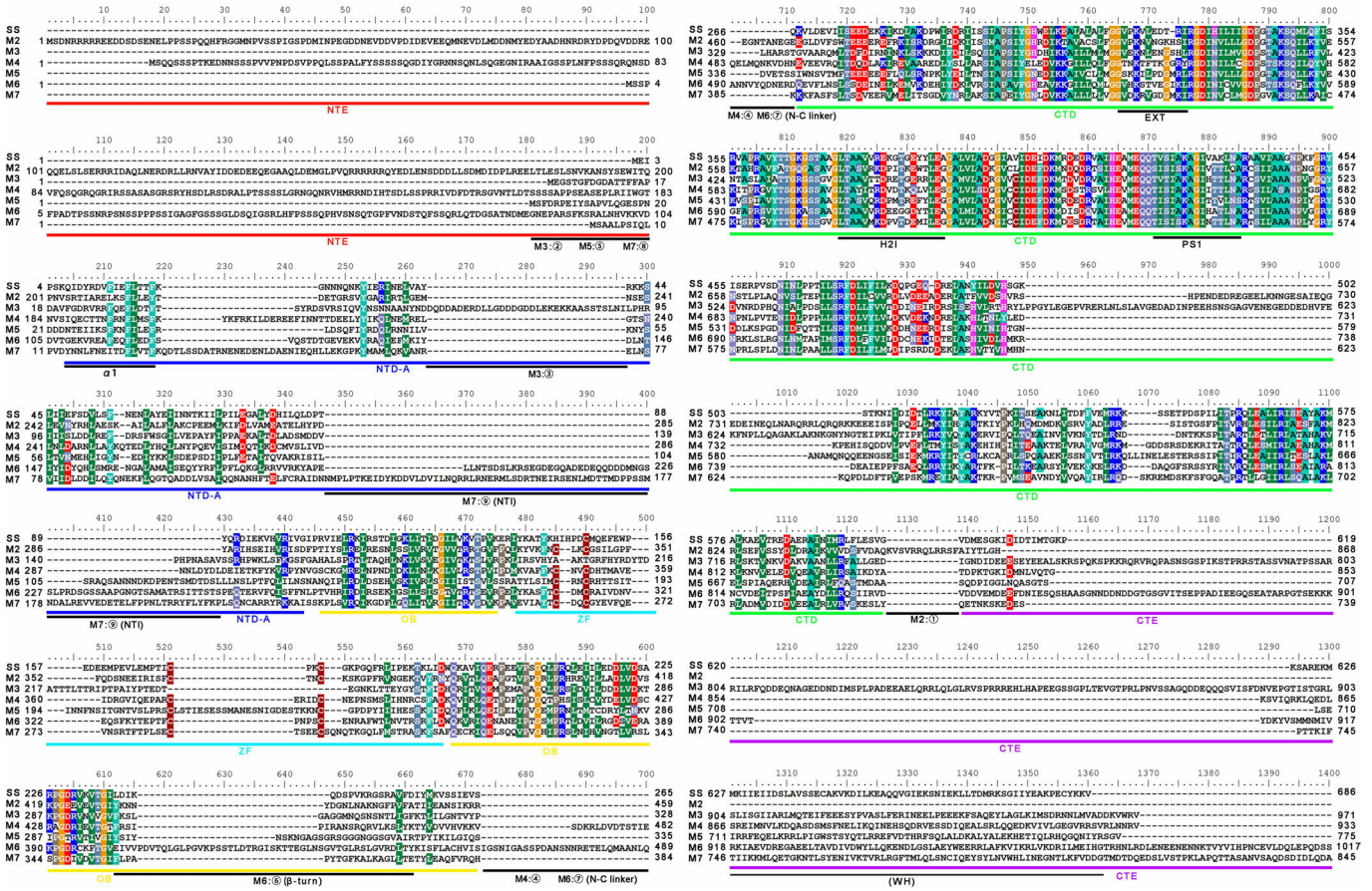

Extended Data Figure 2 | Sequence alignment of the MCM2–7 proteins. The sequences of archaeal (SS, *Sulfolobus solfataricus*) and yeast (*Saccharomyces cerevisiae*) MCM proteins were aligned using BioEdit[73]. The alignment was further adjusted manually according to the secondary structure prediction and 3D structural alignment. Conserved hairpins and loops are labelled (H2I, EXT, PS1 and β-turn). CTEs were aligned by the predicted secondary elements in the winged-helix (WH) motifs. Eukaryote-specific sequences (numbered 1–9) well resolved in our structure as in Extended Data Fig. 4a are labelled.

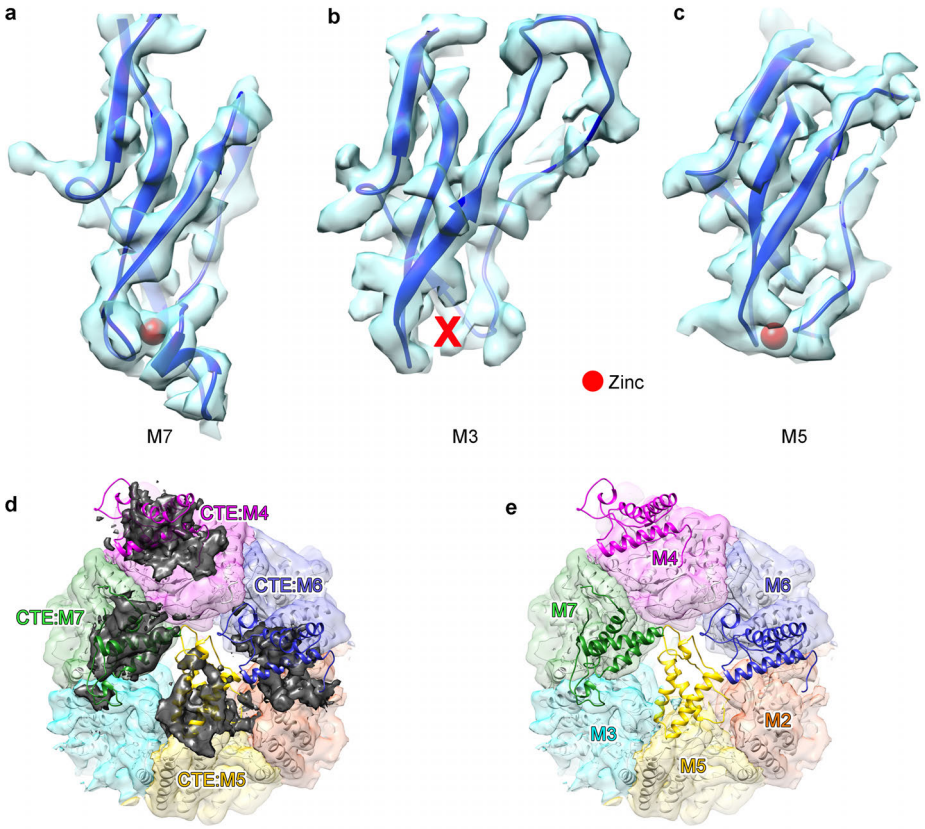

Extended Data Figure 3 | Structural diversity of ZFs and structural flexibility of CTEs in the MCM2–7 double hexamer. **a**–**c**, Ribbon representation of ZF motifs of MCM7 (**a**), MCM3 (**b**) and MCM5 (**c**), superimposed with sharpened density map (transparent cyan) at 4σ contour level. Positions of zinc are denoted by red balls. Zinc-binding was not observed in the ZF of MCM3. **d**, **e**, Surface representation of the density map (unsharpened, at 1σ contour level) superimposed with colour-coded atomic structures for each MCM subunit, viewed from the CTD ring. Four segmented extra densities are coloured in deep grey (**d**), with tentative fitting of a winged-helix motif from a crystal structure (PDB code 2KLQ)[74] into these four density pieces. **e**, Same as **d**, but displayed without extra densities.

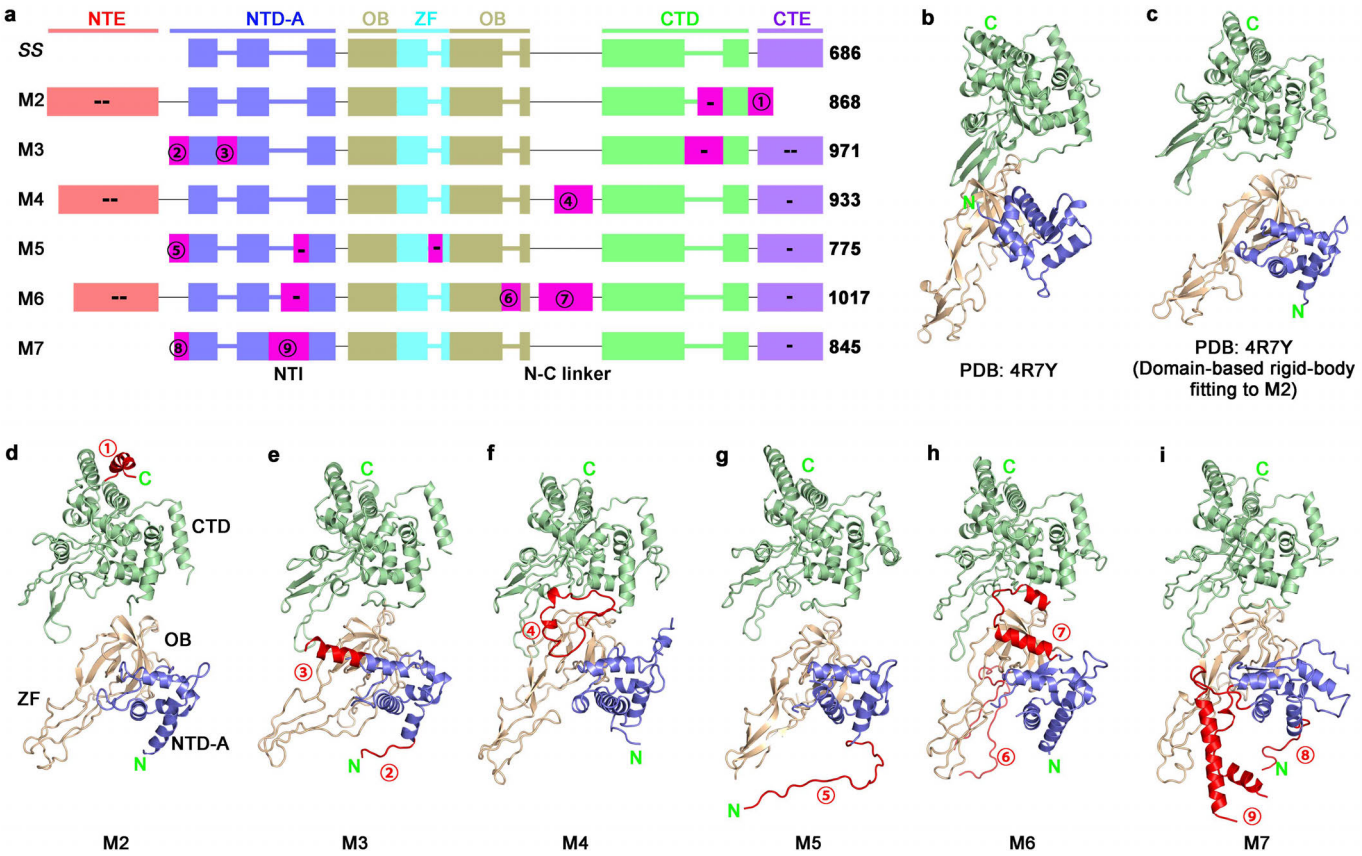

Extended Data Figure 4 | Subunit-specific structural features of the MCM2–7 subunits. **a**, Schematic illustration of domain organization and subunit-specific features of MCM2–7 subunits, with comparison to the archaeal MCM (SS, *Sulfolobus solfataricus*) (see also Extended Data Fig. 2). Numbered regions correspond to numbered extensions and insertions highlighted in **d**–**i**. '-' symbols denote corresponding regions with reliable densities to trace the main chain direction, but not sufficient for atomic modelling. '--' symbols denote sequences with highly disordered densities. **b**, **c**, A protomer of the crystal structure of a chimaeric archaeal MCM hexamer structure (PDB code 4R7Y)[30] used as the template for modelling. The archaeal MCM was aligned globally (**b**) or domain-based flexibly fitted (**c**) to the atomic model of MCM2. **d**–**i**, Side-by-side structural comparison of MCM2–7 proteins, with MCM3-7 globally aligned to the atomic model of MCM2. The well-resolved insertions and extensions of each MCM subunit (**d**–**i**) are numbered and coloured in red.

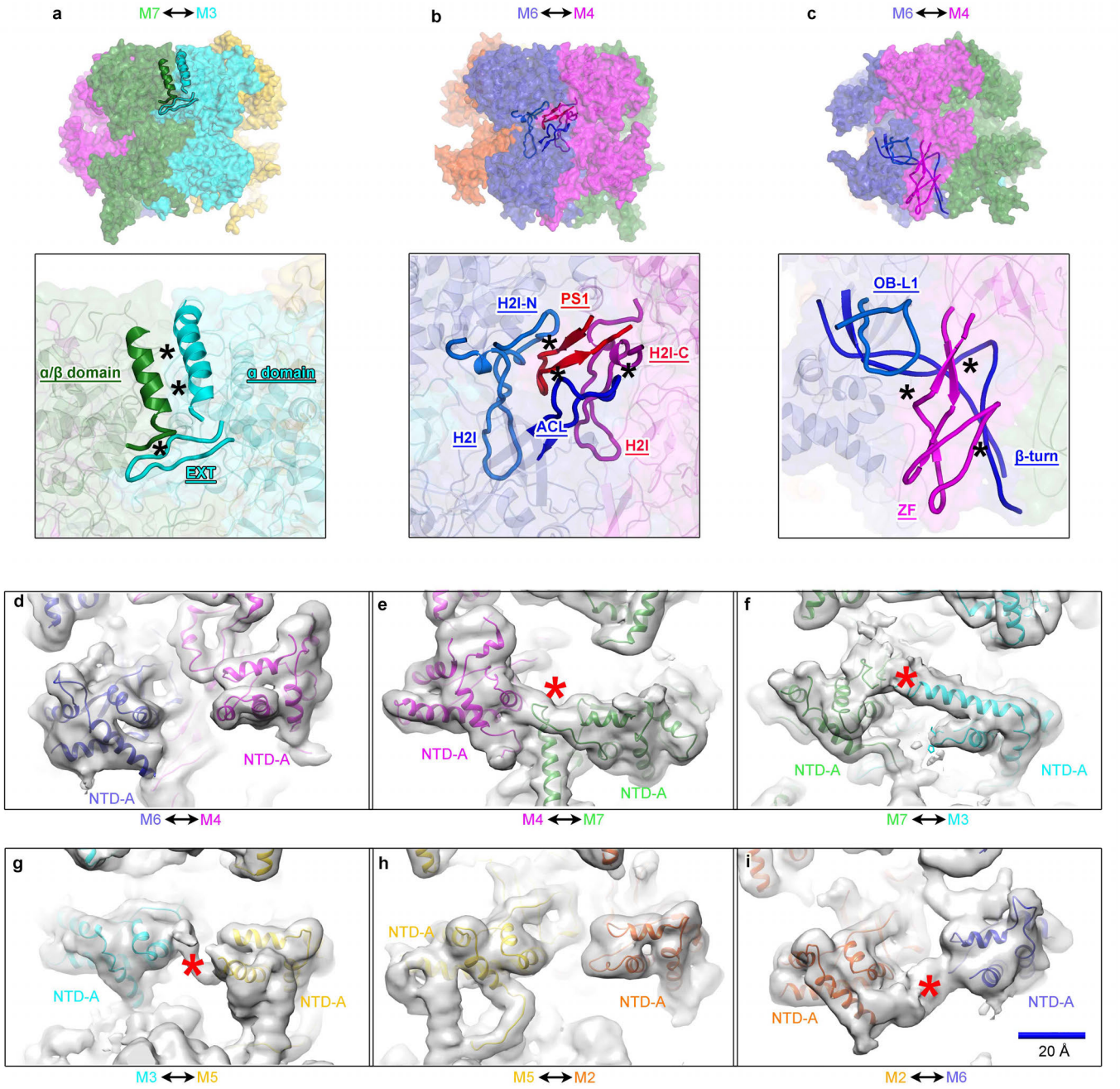

Extended Data Figure 5 | Intersubunit interactions in the MCM2–7 single hexamer. **a**, Interactions at the CTD ring exemplified by the 7:3 interface. The EXT hairpin of MCM3 facilitates the packing of one helix (the α-linker of the α/β subdomain) from MCM7 with another helix (located at the α subdomain of the CTD) from MCM3. **b**, Interactions at the neck region, as exemplified by the 6:4 interface. PS1-HP of MCM4 is sandwiched between ACL and H2I-N (N-terminal loop/helix of H2I) of MCM6. At the same time, ACL of MCM6 also interacts with H2I-C (C-terminal helix of H2I) of MCM4. **c**, Interactions at the NTD ring exemplified by the 6:4 interface. The first loop of OB (OB-L1) that flanks NTD-A, and the extended β-turn loop from MCM6 form a cradle for docking the ZF from MCM4. Asterisks mark sites of strong interactions. **d**–**i**, Zoomed-in views of intersubunit interactions between NTD-As of each adjacent MCM pair. The unsharpened density map (transparent grey), contoured at the 2.7σ level, is superimposed with the atomic model. Four of the six MCM proteins (3, 5, 6 and 7) contain NTIs at varying locations of their NTD-As (see also Extended Data Fig. 4). Only the NTI of MCM7 is modelled in our structure. Superimposition of the atomic model with the density map indicates that these NTIs all interact with the NTD-As of the adjacent subunit on the left. Extra densities indicating interactions are marked by red asterisks.

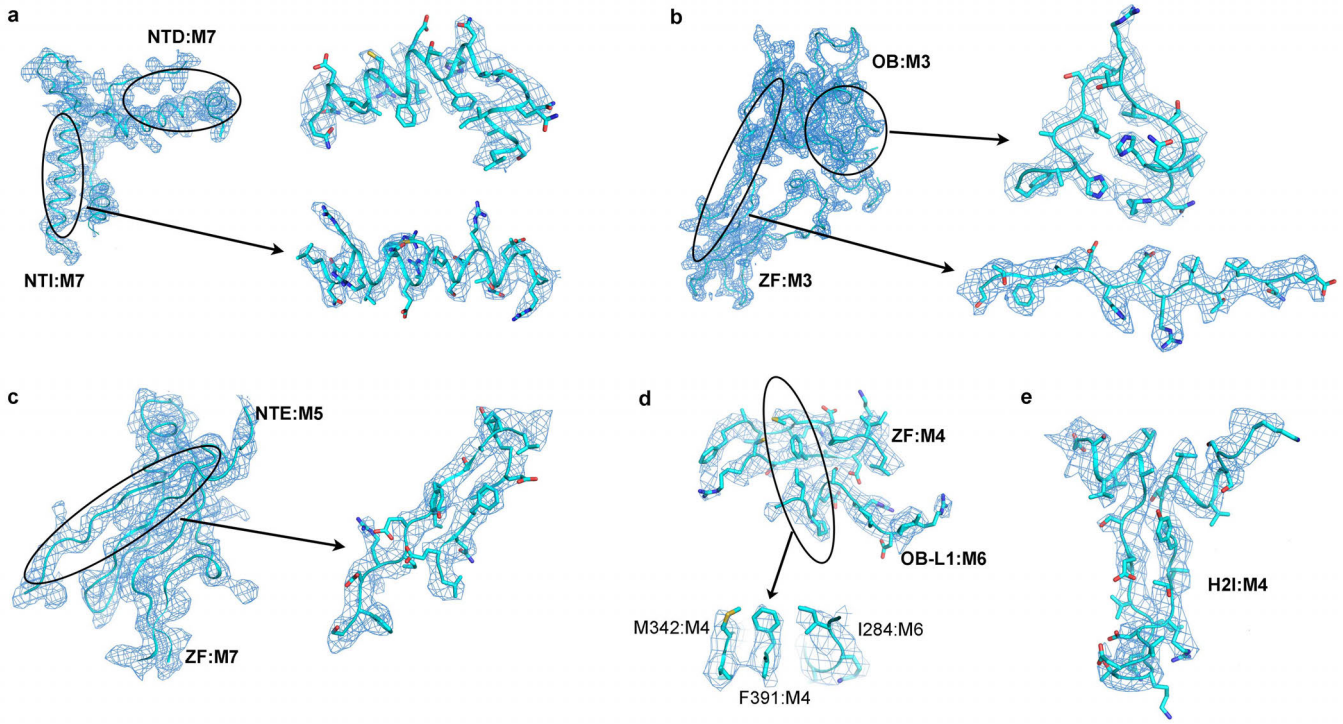

Extended Data Figure 6 | Cryo-EM densities for different regions of the MCM2–7 double hexamer. **a**, Electron microscopy density map (cyan mesh) superimposed with atomic model for NTD-A of MCM7. Two representative α-helices with side chains (right) were displayed in stick representation. **b**, Electron microscopy density map for the OB and ZF of MCM3. A representative loop of the OB and a strand connecting the OB and ZF with side chains are shown on the right. **c**, A representative region of inter-hexamer interaction, highlighting the interactions between the β-strands of MCM5-NTE and MCM7-ZF. **d**, A representative region of intersubunit interaction (MCM4–MCM6), highlighting the hydrophobic interaction between Met342, Phe391 of MCM4 and neighbouring Ile284 of MCM6. **e**, A representative region of conserved hairpin loops, highlighting H2I of MCM4. Segmented density maps in all panels are displayed at the 5–6σ contour level.

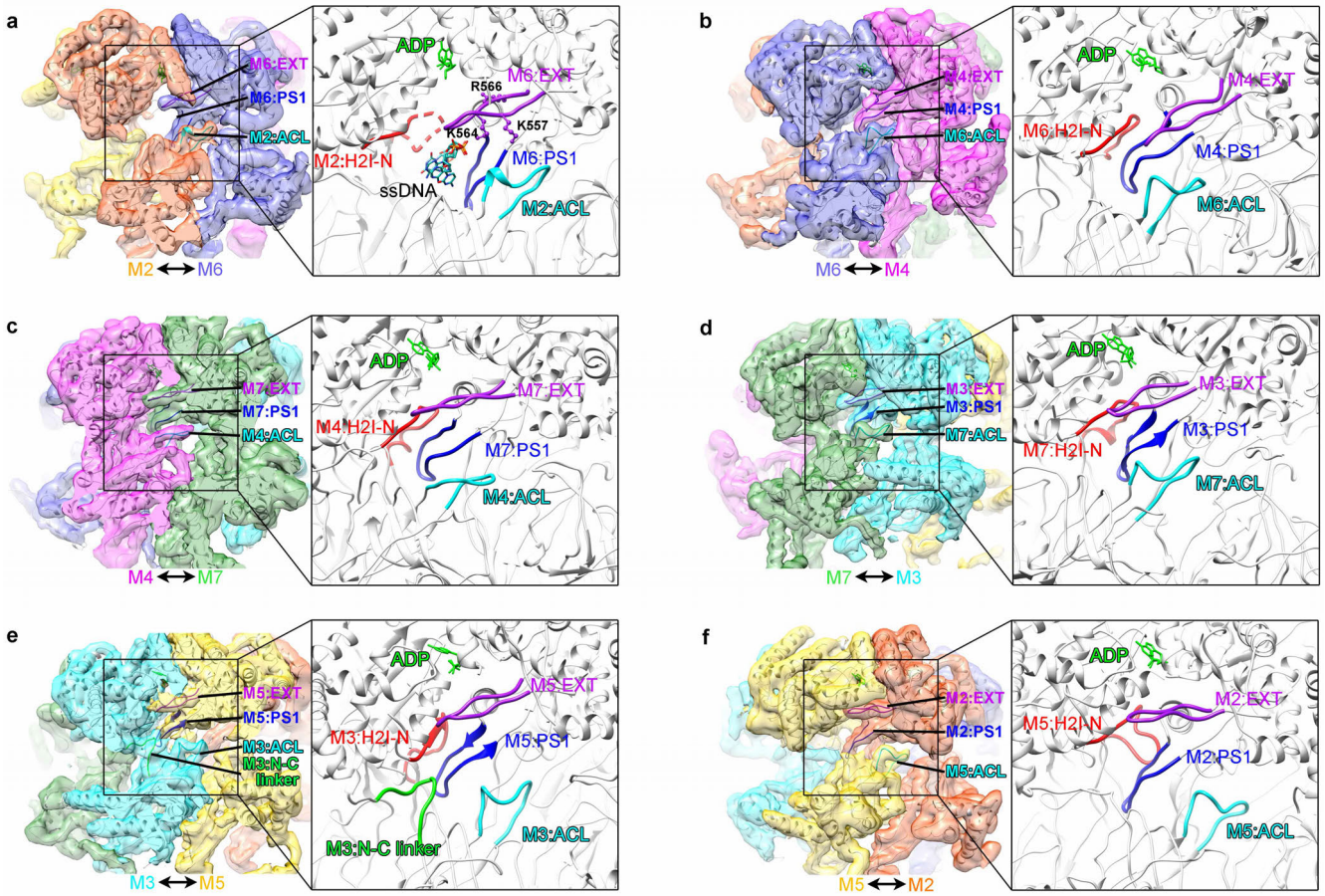

Extended Data Figure 7 | A unique side channel between MCM2 and MCM6. **a**–**f**, Outer surface representation of the six subunit interfaces within MCM2–7 single hexamer. **a**, A unique side channel in the neck region of the M2–M6 interface. The boxed region is shown in a zoomed-in view (right) with individual components (H2I-N, EXT, PS1 and ACL) coloured individually. The size of this side channel is large enough to act as a pore for ssDNA exiting from the central channel during DNA unwinding along with basic residues (Arg566, Lys557 and Lys564) of the EXT hairpin from MCM6. The H2I-N is partially disordered. **b**–**f**, Same as **a**, but at different subunit interfaces. In the case of the 3:5 interface (**e**), the N–C linker of MCM3 also contributes to the blocking of the channel.

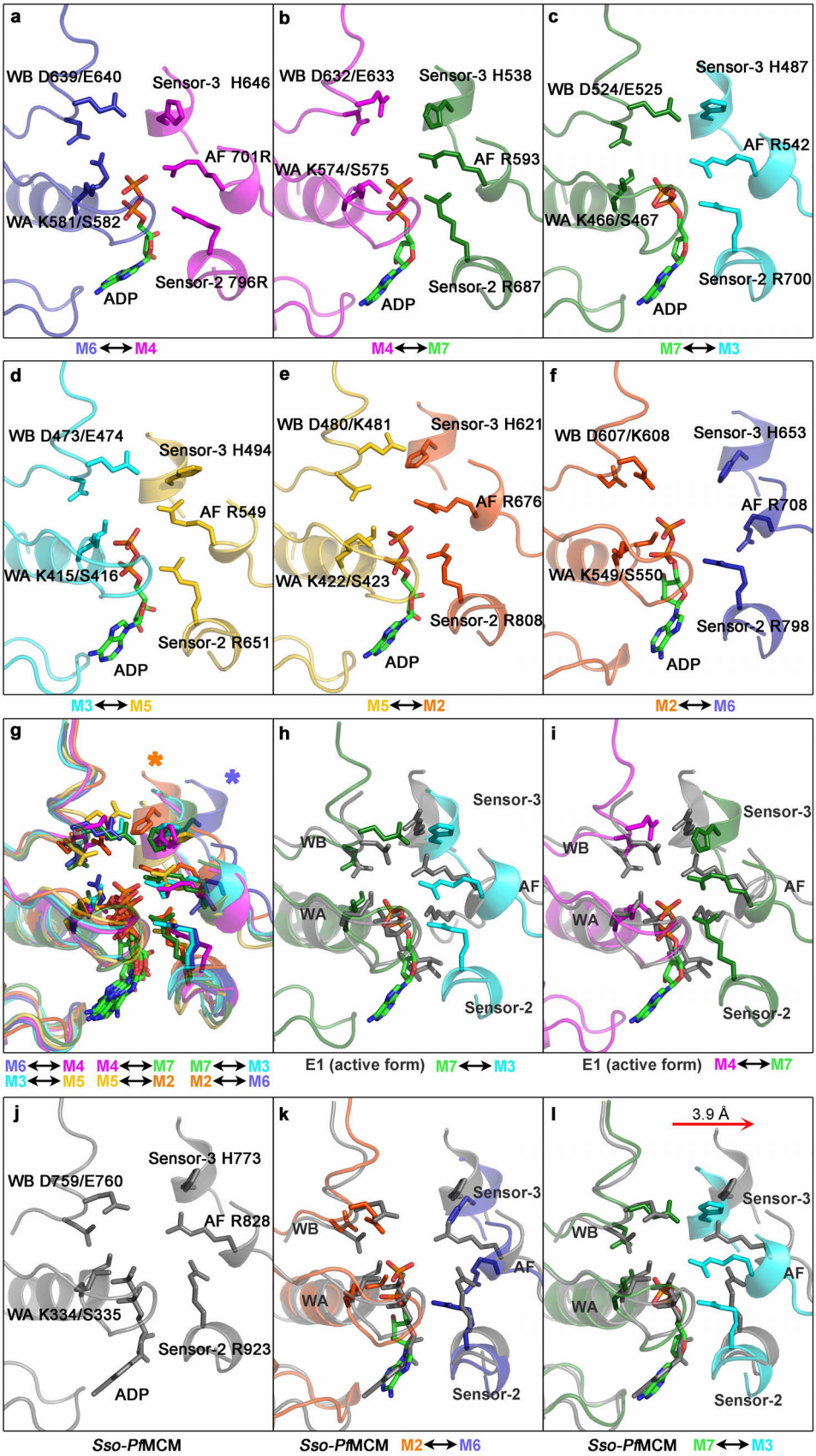

Extended Data Figure 8 | ATP-binding site configuration at MCM intersubunit interfaces. **a**–**f**, Zoomed-in views of ATP-binding sites for each MCM dimer. The Walker A and B (WA and WB, respectively) residues of the left subunit, and sensor 3, sensor 2 and arginine finger (AF) residues of the right subunit, are shown in stick model. **g**, Superimposition of all six active centres. The sensor 3 residues of MCM2 (orange asterisk) and MCM6 (blue asterisk) in the 5:2 and 2:6 dimers display sharply different configurations, resulting in two relatively loose centres. **h**, **i**, Superimposition of two representative compact ATPase centres (dimers of 7:3 and 4:7) with that of E1 hexameric helicase (active form)[40]. **j**, The ATPase centre (inactive conformation) of an archaeal MCM (PDB code 4R7Y)[30]. **k**, **l**, Superimposition of **j** with the centres of 2:6 (**k**) and 7:3 (**l**). Walker A and B motifs are used as a reference for alignment in all panels. **l**, A large shift in the sensor 3 of MCM3 is shown by red arrow, compared with the inactive conformation.

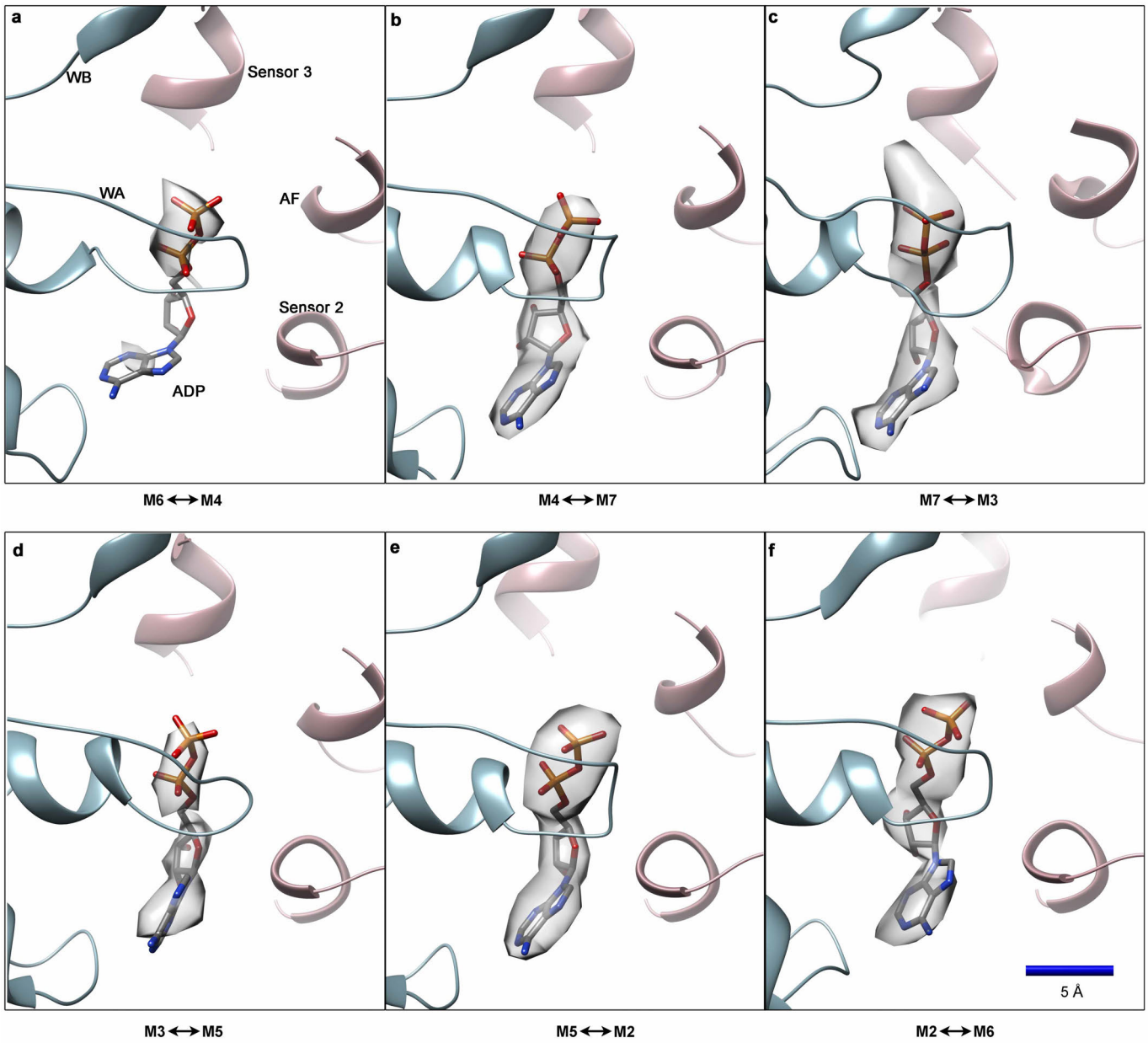

Extended Data Figure 9 | Nucleotide occupancy at the six ATPase centres of MCM2–7 single hexamer. **a**–**f**, Zoomed-in views of the active centres for all MCM subunit pairs. The conserved ATPase elements of the active centres are labelled. Segmented nucleotide densities at a contour level of 5.5σ were superimposed (transparent grey). Note that nucleotide occupancies at the centres of 6:4 and 3:5 are relatively low. For the 7:3 dimer, there seems to be extra density for γ-phosphate or Mg^{2+}, but could not be confirmed at the current resolution (3.8 Å). Nucleotides were modelled using ADP.

Extended Data Table 1 | Statistics of structural determination, model refinement and interface analysis.

a

Buried surface areas for Inter-subunit interactions

Subunits	Buried surface Total (Å²)	Ratio and number of residues involved		Buried surface (Å²)			
		Subunit 1	Subunit 2	Tier 1	Tier 2	Tier 3	Other (N/N, N/ZF, ZF/ZF)
M6/M4	4028	11.5%/114	11.1%/121	1011	1129	1800	230
M4/M7	4122	11.7%/111	10.4%/117	1611	994	1045	591
M7/M3	3825	9.8%/107	11.1%/123	1434	899	893	702
M3/M5	3884	11.4%/107	10.7%/113	1610	1198	994	271
M5/M2	3587	10.1%/103	10.3%/108	1397	1282	999	59
M2/M6	2886	8.6%/78	7.9%/96	1104	869	943	8

Buried surface areas for Inter-hexamer interactions (Å²)

	Total	5:7'/7:5'	3:5'/5:3'	2:6'/6:2'	3:7'/7:3'	3:3'	6:6'	5:5'	4:5'/5:4'	2:4'/4:2'
Total	6387	3284	979	847	625	270	114	102	135	30
ZF:ZF'	981		442	293			114	102		30
N:N'	2272	1487			538	111			136	
N:ZF'/ZF:N'	2531	1748	537		87	159				
β-turn/β-turn'	764	210		554						

Buried surface at the hexamer interface contributed by each subunit

Subunit	M2	M3	M4	M5	M6	M7
Buried surface (Å²)	877	1874	166	4500	961	3909

b

Data collection	
Electron microscope	Titan Krios
Voltage (kV)	300
Electron detector	K2 camera
Electron dose (e^-/Å²)	50 (32 frames)/22 (frame 3-16)
Pixel size (Å)	1.32
3D Reconstruction	
Particles for final refinement	85,366
Resolution of unmasked map (Å)	4.3
Resolution of masked map (Å)	3.8
Map sharpening B-factor (Å²)	-100
Model composition	
Peptide chains	12
Residues	7,572
Ligands (ADP)	12
R.m.s. deviations	
Bonds length (Å)	0.0091
Bonds angles (°)	1.36
Ramachandran plot	
Favored (%)	91.0
Outliers (%)	1.1
Validation	
Molprobity score	2.45
Rotamer outliers (%)	0.06

a, Calculated surface areas of intersubunit and inter-hexamer interfaces. The calculation was done using PISA[72]. At the hexamer interface, there are 25 and 10 residues not built (owing to the structural disorder) for the ZF of MCM5 and the β-turn loop of MCM6, respectively. Therefore, the actual contribution of the MCM5-ZF and MCM6-β-turn to the interhexamer interaction could be much larger. **b**, Statistics of data processing and model refinement.